## LIGHTS. THE EXTENDED POINT SPREAD FUNCTIONS OF THE LARGE BINOCULAR CAMERAS AT THE LBT

Nafise Sedighi <sup>1,2</sup>, Zahra Sharbaf <sup>1,2</sup>, Ignacio Trujillo <sup>1,2</sup>, Sepideh Eskandarlou <sup>3</sup>, Giulia Golini <sup>1,2</sup>, Raúl Infante-Sainz <sup>3</sup>, Samane Raji <sup>4</sup>, Dennis Zaritsky <sup>5</sup>, Pedram Ashofteh Ardakani <sup>6</sup>, Nushkia Chamba <sup>7</sup>, Zahra Hosseini Shahisavandi <sup>8</sup>, Richard Donnerstein <sup>5</sup>, Mauro D'Onofrio <sup>8</sup>, Garreth Martin <sup>9</sup>, Mireia Montes <sup>10</sup>, and Javier Román <sup>11</sup>

<sup>1</sup>Instituto de Astrofísica de Canarias, C/ Vía Líactea,38200 La Laguna, Tenerife, Spain
 <sup>2</sup> Departamento de Astrofísica, Universidad de La Laguna, 38206 La Laguna, Tenerife, Spain
 <sup>3</sup>Centro de Estudios de Física del Cosmos de Aragón (CEFCA), Plaza San Juan, 1, E-44001, Teruel, Spain
 <sup>4</sup> Departamento de Física Teórica, Atómica y Óptica, Universidad de Valladolid, 47002 Valladolid, Spain
 <sup>5</sup>Steward Observatory, University of Arizona, 933 North Cherry Avenue, Tucson, AZ 85721-0065, USA

Steward Observatory, University of Arizona, 933 North Cherry Avenue, Tucson, AZ 85721-0005,

6 School of Astronomy, Institute for Research in Fundamental Sciences (IPM), Tehran, Iran

7 NASA Ames Research Center, Moffett Field, CA 94035, USA

Department of Physics and Astronomy, University of Padova, Vicolo Osservatorio 3, I-35122, Italy
 School of Physics and Astronomy, University of Nottingham, University Park, Nottingham NG7 2RD, UK
 Institute of Space Sciences (ICE, CSIC), Campus UAB, Carrer de Can Magrans, s/n, 08193 Barcelona, Spain and
 Departamento de Física de la Tierra y Astrofísica, Universidad Complutense de Madrid, E-28040 Madrid, Spain
 Version October 29, 2024

#### Abstract

With the arrival of the next generation of ultra-deep optical imaging surveys reaching  $\mu_V \sim 30$  mag/arcsec<sup>2</sup> ( $3\sigma$ ;  $10''\times10''$ ), the removal of scattered light due to the point spread function (PSF) effect remains a critical step for the scientific exploitation of the low surface brightness information contained in these data. Because virtually all pixels in the ground-based images are affected by an unwanted screen of light with a brightness greater than  $\mu_V \sim 29$  mag/arcsec<sup>2</sup>, the characterization of the extended PSF (R>5 arcmin) is mandatory. We describe the procedure used to construct the extended PSFs of the LIGHTS survey in the g- and r-band images taken with the Large Binocular Cameras (LBCs) of the Large Binocular Telescope (LBT). We produce PSFs with a radial extension of 7.5 arcmins. These are later extended to 30 arcmins following an empirically motivated power-law extrapolation of their behaviour in their outermost regions. As an example of the application of our methodology, we subtract the scattered light around the galaxy NGC3198. The result of this subtraction clearly shows the outermost parts of the galaxy's disc, which have been obscured by the influence of nearby bright stars. Following a reproducible science philosophy, we make all the PSF models and the scripts used to do the analysis of this paper publicly available.

Subject headings: Instrumentation: detectors – Methods: data analysis – Techniques: image processing – Techniques: photometric – Galaxies: halos

## 1. INTRODUCTION

During this decade, an increasing number of ultra-deep optical imaging surveys will be able to observe a large part of the night sky down to a surface brightness of  $\mu_V \sim 30 \text{ mag/arcsec}^2$  or even fainter (see e.g. Euclid, LSST; Euclid Collaboration et al. 2024; Watkins et al. 2024; Borlaff & Marcum 2022; Laine et al. 2018). The scientific use of these new images in the very low surface brightness regime ( $\mu_V > 28 \text{ mag/arcsec}^2$ ) will depend on our ability to remove scattered light from the brightest sources in the images. As deeper and deeper images of some regions of the sky have become available (see e.g. Ferrarese et al. 2012; Mihos et al. 2013; Duc et al. 2015; Capaccioli et al. 2015; Fliri & Trujillo 2016; Merritt et al. 2016; Huang et al. 2018; Hood et al. 2018; Rich et al. 2019; Golini et al. 2024), we have come to understand that in ground-based data taken with natural seeing, the effect of scattered light creates a non-uniform light screen that affects the entire image. The intensity of this light

screen depends on the proximity of the emitting sources, but even in regions of the sky with few stars, virtually all pixels in the image are affected by this scattered light at a surface brightness of  $\mu_V \sim 29$  mag/arcsec<sup>2</sup> (see e.g. Slater et al. 2009; Trujillo & Fliri 2016; Montes et al. 2021). For this reason, it is absolutely necessary to eliminate scattered light by constructing point spread function (PSF) models of the images where the PSF extends as far in radius as possible.

In addition to the light screen caused by scattered light, the characterization of the extended PSF of deep images is needed to solve a number of problems in low surface brightness studies. Some examples are the detection of objects with surface brightness comparable to the intensity of the scattered light (see e.g. Haigh et al. 2021; Román et al. 2021, 2023; Montes et al. 2024), the colour estimation of low surface brightness sources (Román et al. 2020), or the analysis of the outer part of galaxies (see e.g. Trujillo & Bakos 2013; Sandin 2014;

Martín-Navarro et al. 2014; Borlaff et al. 2019; Martínez-Lombilla et al. 2019).

We present the characterisation of the extended PSFs (R>5 arcmin) in the Sloan g and r bands of the Large Binocular Cameras (LBC; Giallongo et al. 2008) of the Large Binocular Telescope (LBT). This work is part of the LIGHTS ultra-deep optical imaging survey (Large Binocular Telescope Imaging of Galactic Halos and Tidal Structures; Trujillo et al. 2021; Zaritsky et al. 2024). To date, LIGHTS has observed 25 nearby galaxies (Distance  $\lesssim 20$  Mpc) down to the surface brightness limits of  $\mu_g \sim 31.3$  mag/arcsec<sup>2</sup> and  $\mu_r \sim 30.7$  mag/arcsec<sup>2</sup> ( $3\sigma$  in equivalent areas of  $10\times 10$  arcsec<sup>2</sup>; Zaritsky et al. 2024). This survey is the deepest and most extensive ground-based survey ever undertaken of nearby galaxies and is teaching us important lessons about the handling of very deep data that will be used in the next generation of sky surveys.

To construct the extended PSFs of the LBCs, we follow a similar methodology to that used by Infante-Sainz et al. (2020) to construct the extended PSFs of the Sloan Digital Sky Survey (SDSS; York et al. 2000). That is, we use stars of different magnitudes to generate the PSF across different radial ranges. The brighter (and therefore saturated) stars are used only for the outer part, while the fainter stars are used to generate both the inner and the intermediate parts of the PSF. This paper is organized as follows.

Section 2 gives a brief overview of the data used in this work. Section 3 is devoted to the construction and assembly of the different parts that make up the extended PSFs. In section 4 we show a practical example of how the extended PSFs are used to remove the scattered light from the LIGHTS NGC3198 field. The magnitude system used in this work is AB (Oke & Gunn 1983).

#### 2. DATA

The data used to construct the extended PSFs of the LBCs are from the LIGHTS survey (Trujillo et al. 2021). LIGHTS is currently a survey of 25 nearby galaxies, covering a total area of about 6.25 square degrees (Zaritsky et al. 2024). Each galaxy is observed simultaneously in the g and r bands for a total on-source time of  $\sim 1.5 \,\mathrm{h}$ . The zero point of both filters has been set to 22.5 mag, while the pixel scale of the image is 0.224". The average seeing of the images is  $\sim 1''$ . The limiting magnitudes for point-like sources, computed within a circular aperture with a radius equal to the Full Width Half Maximum (FWHM) of an unresolved source, in the g and r bands are  $\sim 27.5$  and  $\sim 26.6$  mag  $(5\sigma)$ , respectively. Stars brighter than magnitude 19 are saturated in both filters (the on-source exposure time of the individual frames that make up the LIGHTS mosaics is 3 min). Therefore, such bright stars are only used to construct the intermediate and outer parts of the extended PSFs.

Due to the nature of the survey, the presence of bright stars is avoided as much as possible in the selection of the observed fields (see Zaritsky et al. 2024, for further details). For this reason, the number of bright stars whose characterisation allows us to construct PSFs that are as extended as possible (i.e. with radii  $\sim$ 5 arcmin comparable to the diameter of the studied galaxies given by the location of the isophote  $\mu_V$ =26 mag/arcsec<sup>2</sup>) is limited. In the following sections, we explain the procedure used

to construct such extended PSFs.

#### 3. CONSTRUCTING THE EXTENDED LBC PSFS

Due to the observing strategy of the LIGHTS survey, it is not possible to construct an extended PSF with a single star. As mentioned above, stars brighter than magnitude 19 are saturated (in both filters). Therefore, if we want to characterize the full radial distribution of the PSF from the innermost arcseconds out to arcminute scales. we need to use stars with a wide range of magnitudes. To this end, we have used up to 4 different magnitude ranges, with the aim of obtaining the most accurate characterisation of the entire PSF in terms of signal-to-noise ratio. In the following, the magnitude we quote corresponds to Gaia's G-band filter. We have used the values quoted in the eDR3 release (Gaia Collaboration et al. 2021). G-band was chosen for two reasons. The first is that we need to refer to unsaturated magnitudes, and for our brighter stars, the g and r band values will not be reliable due to their saturation. The other reason is the simplicity of the procedure. The G-band is broad enough to cover both the g and r Sloan filters, so the magnitudes given in this filter are representative of the value of these stars in both Sloan filters.

The central (core) regions of the global PSFs are made up of unsaturated stars with magnitudes between 20 and 21 mag. This range is useful for describing the PSF within a radius of  $\sim 2''$ . From 2" to 16", a part we have called the intermediate region of the PSF, we use three different magnitude ranges: 17 to 18 mag ( $\sim 2''$  to  $\sim 7''$ ), 13 to 15 mag ( $\sim 7''$  to  $\sim 13''$ ) and 9 to 12 mag ( $\sim 13''$  to  $\sim 16''$ ). Finally, the outermost parts of the PSFs are built using one of our brightest stars (7 mag), giving us radial coverage from about  $\sim 16''$  to  $\sim 450''$ . For distances greater than this, we have to extrapolate the behaviour of the PSFs. The following sections describe in detail how we build the different parts of the PSFs and how we merge them into a common and global PSF.

## 3.1. Constructing the outer (16" to 450") part of the PSFs

As mentioned above, the selection of LIGHTS fields (Zaritsky et al. 2024) avoided as much as possible the proximity to bright stars. For this reason, it is difficult to find a sufficiently bright and isolated star that both avoids the central galaxy and is as far as possible from the edge of the image. After visually inspecting all LIGHTS fields, we found a suitable candidate with which to determine the outer part of PSF. The star is HD 134023 (R.A.=15:05:23.7; Dec=+55:40:38.3; J2000; G-band=7.6 mag) and is located in the field of the galaxy NGC5866 (see panel (a) in Fig. 1). Fortuitously, this field has been observed during two observing campaigns and is one of our deepest fields with a total time on the source of 3.1 h and limiting surface brightnesses of  $\mu_q \sim 32$ mag/arcsec<sup>2</sup> and  $\mu_r \sim 31.2$  mag/arcsec<sup>2</sup>  $(3\sigma; 10'' \times 10'')$ . The construction of the outermost part of the PSF is a two-step process.

#### 3.1.1. First step

We start by cutting an area of  $9\times9$  arcmin centred on HD 134023 (see panel (b) in Fig. 1). While the scattered light from the PSF of this star extends beyond this

boundary, the size of the area is chosen to minimise the effect of the light from the central galaxy (NGC5866) and the edge effects of the image. In the selected area, the star is the brightest object, but there are other fainter sources that need to be masked out to get a more accurate representation of the PSF. To build the masks of the contaminating objects we use NoiseChisel followed by Segment (Akhlaghi & Ichikawa 2015a; Akhlaghi 2019). In addition to this automatic mask generation, to be conservative, we augment the masks for the brightest contaminants. Three of these correspond to the three brightest targets around HD 134023 (two stars and one galaxy). These masks are shown as white circles in panel (c) of Fig. 1. The fourth corresponds to the central galaxy (NGC5866). This mask appears in panel (c) as the white area in the upper left corner.

Taking advantage of the circular symmetry of the LBT telescope's PSF, we obtain the radial profile of the PSF using the non-masked pixels employing astscript-radial-profile (Infante-Sainz et al. 2024). Using this first version of the radial profile (see Fig. 2; left panel), we build a preliminary circular 2D PSF model, also with the help of Gnuastro tools. This model is flux normalised in the radial interval from 22.4" to 44.8"(i.e. 100 to 200 pixels). This range is chosen to avoid the saturated part of the star and to minimise contamination from background sources. Once the model was created, we subtracted it from the real star. The result is shown in panel (d) of Fig. 1.

Subtracting the first version of the model from the outer part of the PSF reveals a large number of structures that may affect the properties of the outer surface brightness profile of the PSF. We therefore re-run Gnuastro's tools on this residual image, shown in panel (d), to mask this contamination more effectively. The detection of the low surface brightness structures that affect the determination of the PSF's external shape is shown in panel (e). The resulting new masks are shown in panel (f).

#### 3.1.2. Second step

The improved masking, shown in panel (f) of Fig. 1, allows us to construct a new radial profile that is significantly less affected by low surface brightness contamination around the bright star. The new profiles are shown in Fig. 2. Note that the new profiles generally have fewer counts at a given radial distance than the original ones. This is due to the improved masking, which removes contamination from other sources. The effect is particularly significant in the outermost region of the PSF (right panel of Fig. 2). In these regions, the effect of the contamination was particularly strong due to the proximity of the galaxy NGC5866 and other objects.

Bleeding, due to saturation of the bright star, also affects the outer part of the recovered PSF. In Fig. 1 the regions affected by bleeding can be seen as vertical spikes starting from the centre of the PSF. These regions are also masked when the outer parts of the PSFs are created. The procedure followed so far allows us to construct the region of the PSF that extends from about

Num	Field	RA	Dec	G (mag)
1	NGC5248	204.50033	9.06079	10.83
2	NGC5248	204.57361	8.78941	10.98
3	NGC5248	204.30708	8.73974	11.25
4	NGC5248	204.58561	9.05267	11.30
5	NGC5248	204.48749	8.76922	12.04
6	NGC3941	178.41789	37.04541	10.79
7	NGC6015	238.14633	62.31770	9.19

TABLE 1
THE LIST OF SELECTED STARS FOR CONSTRUCTING THE OUTER
INTERMEDIATE PART.

16'' to 450''. In the following, we will explain the generation of the PSF in the inner (R<16'') parts.

# 3.2. Constructing the intermediate part (2" to 16") of the PSFs

The construction of the intermediate part of the PSF is divided into three different radial ranges. The selection of the different radial ranges is a compromise between the radial extension of the saturated core of the stars, which scales with their magnitude, and a similar signal-to-noise when averaging the profiles at different radial locations.

## 3.2.1. Outer intermediate part (13" to 16").

To generate this region of the PSF we used stars in three fields (NGC3941, NGC5248, and NGC6015) that have relatively large regions of the field of view free from contamination by very bright sources. We select stars with G-band magnitude between 9 and 12 mag and far (R>36") from other bright sources of equal or greater magnitude. This "isolation" criterion ensures that contamination of the PSF is not an issue in the range of interest (i.e. 13" to 16").

Using the above criteria, seven stars were selected for the outer intermediate region of the PSF. Their positions and magnitudes are given in the Table 1. The process of stacking them to obtain a common PSF is as follows. First, we make an image of  $34''\times34''$  centred on each star. We normalise the radial fluxes among stars using the values from 12'' to 16''. Once the PSFs are normalised, we combined the 2D images of the stars using a resistant mean to avoid potential  $(3\sigma)$  outliers.

We show the result of stacking this part of the PSF in the first row of Fig. 3. The vertical white areas correspond to regions that are masked (during the stacking process) due to the presence of bleeding (associated with the saturation of the stars), as happened with the outermost part of the PSF shown in the previous section.

### 3.2.2. Middle intermediate part (7" to 13")

The process of constructing this part of the PSF follows the same procedure as for the outer intermediate region, but using 63 stars in the magnitude range of 13 to 15 (G-band). We used the 18 fields of the 25 current LIGHTS fields that were fully reduced at the time of this work. The normalisation annulus used to bring all the stars to

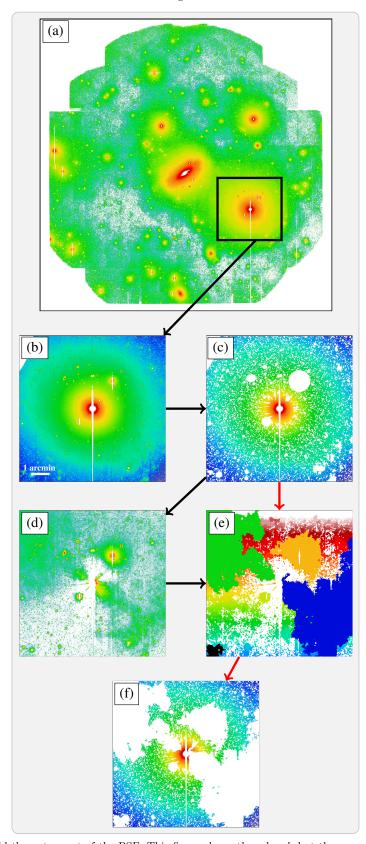


FIG. 1.— Steps taken to build the outer part of the PSF. This figure shows the g-band, but the procedure is also valid for the r-band. Panel (a) shows the position of the star HD 134023 within the LIGHTS field of the galaxy NGC5866. Panel (b) displays the area selected to create the PSF outer region. Panel (c) shows the first step of the mask. A preliminary model of the outer part of the PSF is subtracted from the real star to better characterise the contamination of the background around the star (panel (d)). In panel (e) we show the segmentation map generated by NoiseChisel and Segment applied to the subtracted image from (d). Finally, in panel (f) we show the new masked region, which is a significant improvement in terms of the ability to mask the contaminated areas shown in (d) compared to the original masked region shown in (c).

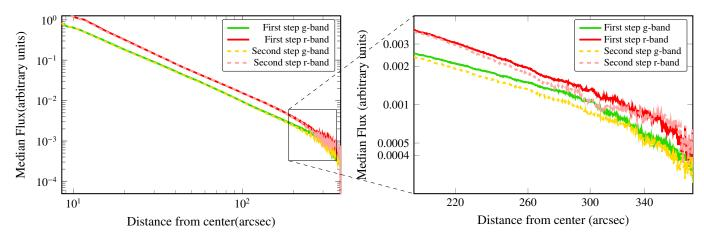


Fig. 2.— Radial profiles of the outer region of the PSF of the LBC camera in the g- and r-band filters. The left panel shows how the shape of the radial profile changes after different masking steps. The right panel zooms in on the outermost region to better visualise the effect of masking contamination from nearby sources.

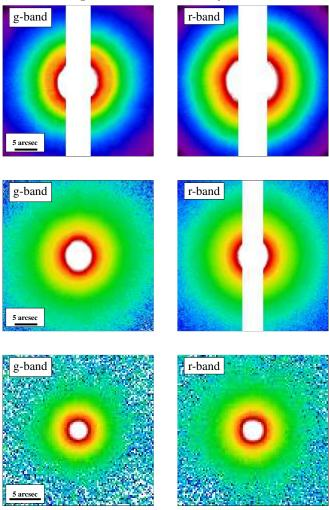


FIG. 3.— The stacked images of the intermediate parts of the PSFs. The stacked images are in the following order. First row: outer intermediate region (13'' to 16''). Second row: middle intermediate region (7'' to 13''). Third row: inner intermediate region (2'' to 7''). Each stamp has its own colour range to make it easier to see the different parts of the PSF.

the same flux was from 9'' to 11''. The result of stacking the images of these stars is shown in the second row of Fig. 3.

### 3.2.3. Inner intermediate part (2'' to 7')

For this part of the PSF, we used 76 stars in the magnitude range of 17 to 18 mag (G-band). As before, we used 18 of the 25 LIGHTS fields. Because these are fainter stars, we do not lack candidate sources but need to avoid contamination of bona-fide point-like sources (i.e. stars) produced by compact background objects, such as high redshift galaxies. We add an additional criterion and require Gaia sources in this magnitude range to have a parallax measurement that is at least three times larger than the associated uncertainty. Moreover, we request the axis ratio to be at least 0.9. We use the radial range from 4.5'' to 9'' to normalise the profiles. The result of stacking the images of these stars is shown in the bottom row of Fig. 3. In Fig. 4, we show the radial profiles in both g and r Sloan filters of the different radial ranges of the PSFs.

## 3.3. Constructing the core (0" to 2") of the PSFs

To create the innermost part of the PSFs we followed the previous steps using stars with G-band magnitudes between 20 and 21. Stars in this magnitude range do not show saturation in either our g and r filters. We are more conservative in selecting stars rather than background galaxies. We add the additional requirement that the axis ratio be greater than 0.93.

We take an additional measure to remove binary stars. We exclude any star that belongs to the Washington Double Star (WDS) catalogue (Mason et al. 2012), which contains a list of 141000 known binary stars. To be even more conservative, we remove any star that has another object within 90" that is brighter than 25 mag in the LIGHTS catalogue (i.e. in the relevant g-band or r-band). We are left with a total of 92 and 95 stars in the g and r bands, respectively, to combine to form the core.

To recover the core of the PSF, we mask all the contaminant sources within a radial range of 7'' to our selected stars. We normalise the fluxes of each of our stars using the values within 1'' to 2'' prior to recovering the stacked radial profile. The final stacked images representing the

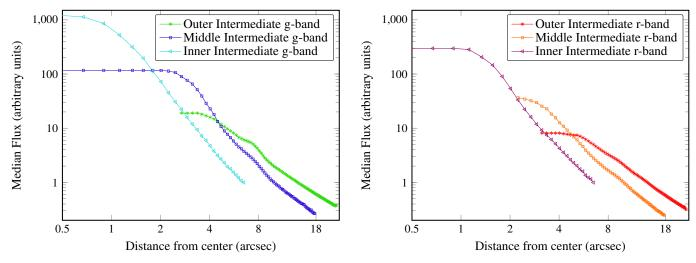


Fig. 4.— The radial profiles of the intermediate parts of the PSFs in the g (left panel) and r (right panel) Sloan bands. The different fluxes are indicative of the different magnitude ranges used to construct these different radial parts of the PSFs.

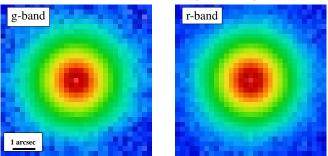


Fig. 5.— The stacked images of the core part of the LBC PSFs in the g and r Sloan filters.

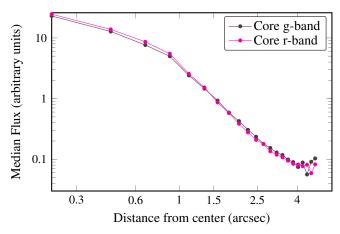


Fig. 6.— The radial profiles of the core of the LBC PSFs in the  ${\bf g}$  and  ${\bf r}$  Sloan bands.

core of the PSFs are shown in Fig. 5 and their radial profiles in Fig. 6.

### 3.4. Building the global PSFs

Once the process of constructing the five parts of the PSF is complete, we produce a single PSF resulting from the assembly of the different regions. We select a radial range where the outer intermediate and outer PSFs

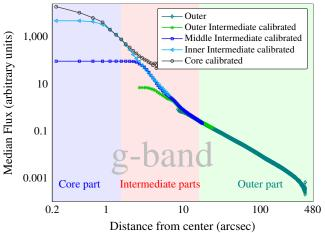


Fig. 7.— Building the global g-band PSF of the LBC camera of the LBT. The profiles of the different parts of the PSF are matched in different regions.

have comparable S/N (i.e. 15.7" to 19"). This matching is necessary to ensure a smooth transition between the different parts of the PSF. Once the outer intermediate and outer parts of the PSF have been joined, the process is repeated with the remaining parts of the PSF until the whole PSF is complete. Fig. 7 and Fig. 8 show the radial regions (11.2" to 15.7", 4.9" to 7.2" and 1.3" to 2") where the different parts of the PSFs have been joined. The images including the different parts of the PSFs are shown in Fig. 9. The white areas correspond to the regions that have been masked due to the presence of nearby contaminants, as explained above (see section 3.1.1). Fortunately, the optical path of the LBT telescope has few elements that disturb the symmetry of the PSFs. Therefore, they do not deviate significantly from circular symmetry. For this reason, it is possible to use the radial profile of the PSF to build a complete two-dimensional PSF model, filling in the gaps due to masking. In the next section, we will explain the circularisation process and how to extend the PSF radially.

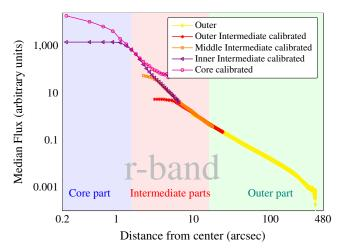
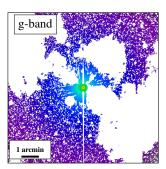


Fig. 8.— Building the global r-band PSF of the LBC camera of the LBT. The profiles of the different parts of the PSF are matched in different regions to allow a smooth transition.



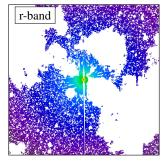


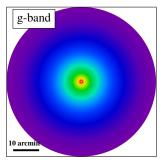
Fig. 9.— The 2D image of the LBC PSFs in the g- and r-bands. The white areas correspond to masked areas due to contamination from nearby sources or bleeding.

#### 3.5. Creating the extended PSFs

To fill the empty regions where we lack information due to the presence of nearby sources, we take advantage of the circular symmetry of the LBC PSFs. This allows us to use the radial profile of the PSFs and fill the empty regions with the average flux at a given radial distance.

In this work, the radial extent of the measured PSFs is ultimately limited by the brightness of the brightest star used to construct the outer part of the profile. Considering the depth of our survey in this region, this allows us to obtain profiles for the PSFs that extend up to 450". Although measuring the PSF to this extent may seem adequate, it is insufficient for some of the galaxies. Following the criterion suggested by Sandin (2014), one would like to have PSF models that are at least 2 times larger than the extension of the object of interest. For this reason, and also to be able to remove all the scattered light in our field of view, which is about 30 arcmin on each side, we decided to extend the outermost part of the PSF radially, following the slope of the outer part of the observed PSF. This extension of the PSFs beyond a radial distance of 7.5 arcmin is undoubtedly the most speculative part of our work. In the following, we justify our choice of procedure for such an extension.

To extend the radial profile of the PSFs beyond 7.5 arcmin, we assume that the PSFs follow the same slope as



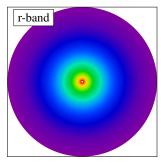


Fig. 10.— Circularised and extended to a radial range of 30 arcmin of the g- and r-band PSFs of the LBC cameras of the LBT telescope.

that observed in the outer region (R>50") of the current PSF models. This assumption is motivated by the outer shape of the large collection of PSFs given in Fig. 1 by Sandin (2014). Sandin (2014) shows that in the "aureole" region<sup>1</sup>, the slope of the PSFs for different telescopes and filters is well approximated by a power-law behaviour. We fit a power-law to the PSFs over the radial range from 110" to 225". This range is a compromise between having high signal to noise of the outer part of the PSF profile and potential problems of over-subtraction of the background affecting the outermost regions of the PSFs.

For the g-band, we found a slope of  $-2.1\pm0.1$ , while for the r-band the slope is  $-2.1\pm0.2$ . The uncertainties are estimated based on the variation in the recovered slope when making minor changes to the radial fitting range. Values for the outer PSF slope from ground-based images between -2 and -3 are common in the literature. For example, Infante-Sainz et al. (2020) found a slope of -2.5 for SDSS PSFs. Trujillo & Fliri (2016) got -2.1 (rband), while Mancera Piña et al. (2024) got -2.9 (g-band) and -2.55 (r-band) for the GTC new OSIRIS camera, while for Gemini telescopes Golini et al. (2024) got -2.6 for g-band and -2.75 for r-band. We caution that the measured slope of the outer PSFs obtained using images dedicated to the study of galaxies that fill the central part of the image are necessarily steeper than the real slope of the PSF. This is due to the pipeline processing of the image, which, although designed to minimise the effect of background over-subtraction, is necessarily affected by scattered light. Finally, assuming the slopes we have measured above for the LBT telescope, we extend the PSFs up to 30 arcmin. These circularised and extended profiles are shown in Fig. 10. The radial profiles are provided in Fig. 11.

## 4. USING THE GLOBAL PSF TO REMOVE SCATTERED LIGHT IN THE NGC3198 FIELD

We perform the practical exercise of removing the scattered light from the LIGHTS NGC3198 field using our extended PSFs. This field is particularly attractive for this exercise because the central galaxy is affected by scattered light from several nearby stars at its edges (see Fig. 12).

 $^1$  Sandin (2014) describes the aureole region as the radial range of the PSF between  $30^{\prime\prime}$  to 1.5 degrees.

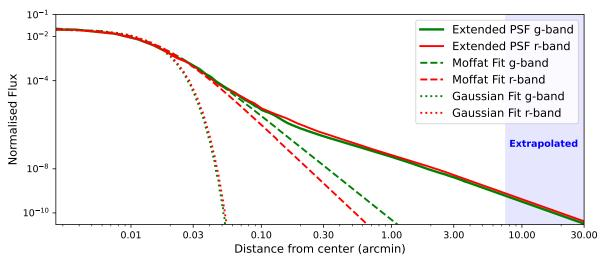


Fig. 11.— Circularised and extended radial profiles of the g- and r-band PSFs from the LBC cameras on the LBT telescope. The region measured from stars directly in the image corresponds to R<7.5 arcmin. Beyond this radius, the PSFs have been extrapolated assuming a power-law decay with a slope of -2.1 for the g- and r-bands. We include both the Gaussian (FWHM $_g$ =1.15±0.05" and FWHM $_r$ =1.18±0.05") and the Moffat (FWHM $_g$ =1.00±0.05",  $\beta_g$ =2.4±0.1 and FWHM $_r$ =1.04±0.05",  $\beta_r$ =2.8±0.1) profiles after fitting these functions to the global PSF models. These fits show where traditional approaches to modelling the PSFs (see e.g. Trujillo et al. 2001a,b) start to deviate (~1.5" for Gaussian and ~3" for Moffat fits) from the extended PSFs.

To construct the scattered light image in the field, we model the contribution from all stars in the field with magnitude G-band < 17 mag. The choice of magnitude is somewhat arbitrary and can be extended if necessary. We also do not model bright stars outside the field of view of this image. While this is possible, a visual inspection of the area around this galaxy using SDSS data beyond the area covered by LIGHTS shows no bright stars affecting the outermost part of the field. Therefore, for the purposes of this exercise, we consider this to be sufficient. A total of 133 stars are then modelled. The positions of these stars (all saturated) in the images are taken from the Gaia catalogues. This works because the Gaia catalogues and the LIGHTS images were taken only a few years apart.

The modelling of the scattered light field followed a hierarchical approach, starting with the PSF fitting and subtraction of the brightest star. This was then repeated for the second brightest star, and so on. This iterative procedure was necessary because the light emitted by very bright stars significantly affects the fitting and subtraction of nearby, fainter stars. The PSF fitting of each star involved two steps: the determination of the centre of the star and the flux calibration of the PSF model to the light profile of the star. The first is solved using the coordinates from the Gaia catalogue. To calibrate the PSF model to the brightness of each star, we use the radial surface brightness profile of each star. Since the brightness varies, we cannot use a fixed radial range to perform the calibration for all stars, as it could be affected (depending on the star's magnitude) by the saturation region or a poor signal-to-noise ratio. For this reason, the selected range of the star's profile is given by the surface brightness range between 22.5 and 25 mag/arcsec<sup>2</sup>. This range is common for both g and r bands. Given the properties of the LIGHTS survey, this surface brightness range skips both the saturation brightness ( $\sim 21.3~\text{mag/arcsec}^2$  in g and  $\sim 20.3~\text{mag/arcsec}^2$  in r-band) and the limiting surface brightness (31.3 mag/arcsec² in g and 30.7 mag/arcsec² in r-band). Once the radial range of each individual star is selected based on the common surface brightness range, we calculate the ratio F between the counts of the surface brightness profiles of the real stars and the PSF models. The ratio F is calculated using a  $3\sigma$  clipped mean to avoid the effect of potential outliers. With the star's central position and F determined, each star was fully modelled and then subtracted from the original image. This process was repeated for each star until the final faintest star considered for the scattered light map of the image was modelled and subtracted.

In the middle panel of figure 12 we show (in colour) the scattered light field produced by the brightest stars in the field. Note that the calibration performed produces satisfactory results in modelling not only the appearance of the scattered light but also the colours of the modelled stars. The subtraction of this scattered light produces an image (see Fig. 12 bottom panel) that is almost free of light contamination from the bright stars in the field of view of the galaxy under study. Once the scattered light has been removed, it is easier to see the degradation of the signal-to-noise ratio towards the edge of the image (darker areas), artifacts during the reduction process, and some residuals in the core of the brightest stars, since the PSF models by construction have neither saturated cores nor bleeding problems. This scattered lightfree image also gives us the opportunity to explore the edge (see e.g. Trujillo et al. 2020; Chamba et al. 2022) of NGC3198 with unprecedented accuracy.

Having the scattered light map allows us to quantitatively explore the amount of light contamination due to the PSF effect on the nearby sources at the location of the central galaxy. In Fig. 13 we show this for the g-

band filter. In the centre of the panel, the scattered light contributes with a screen of about  $28.9 \text{ mag/arcsec}^2$ . In the case of the r band, the scattered light map has a similar structure and the contamination in the centre is  $28.1 \text{ mag/arcsec}^2$ . Interestingly, also the colour of the scattered light at the central part of the field (g-r)<sub>0</sub>=0.8 mag barely changes when adding enough stars to model it. At the edge of NGC3198, due to the distribution of the bright stars, the scattered light contamination is more important and reaches surface brightness levels comparable to the surface brightness of the outer disc of the object, making its study more complex.

A final test we can perform is to examine the contribution of the scattered light to the surface brightness in the central region of the image as a function of the magnitude of the stars being modelled. In Fig. 14 we show how the surface brightness of the scattered light becomes brighter as fainter and fainter stars are added to model the scattered light of the field. For this particular field, the contribution to the central surface brightness remains almost unchanged (<3%) when stars fainter than 16 (G-band) are added to the model. For other fields, with stars of different magnitudes and/or at different positions in the image, the shape of the curves shown in Fig. 14 will of course be different.

#### 5. CONCLUSIONS

The new generation of ultra-deep optical sky surveys is designed to routinely obtain images with surface brightnesses of  $\mu_V \sim 30 \text{ mag/arcsec}^2$  or fainter. One of the main problems facing the analysis of these images is the contribution of light scattered from the bright sources. As shown in the present paper, but also in previous work with ground-based data (e.g. Slater et al. 2009; Trujillo & Fliri 2016; Montes et al. 2021), it is difficult for this contamination not to reach surface brightnesses of  $\mu_V \sim 29 \text{ mag/arcsec}^2$ , even in areas relatively far away from bright sources. This value is therefore brighter than the limiting surface brightness of the images and prevents full use of the data if not corrected. To overcome this problem, ultra-deep surveys must therefore characterise the extended PSF of their images with great care. In this paper, we show how this process has been carried out in the context of the LIGHTS survey with the LBT.

We have applied the methodology developed by Infante-Sainz et al. (2020) to the g- and r-band images of the LIGHTS survey. The characteristics of the survey allowed us to construct the PSF directly from the data up to 450". While this extension is remarkable, it is insufficient to address our need to characterise the scattered light contribution in the full field of view of the LIGHTS mosaics ( $\sim 30$  arcmin on the side). For this reason, we extrapolate the behaviour of the PSFs from 7.5 arcmin to 30 arcmin. This extrapolation is justified by the behaviour of other extended PSFs taken from ground-based data.

Finally, as a practical example, we show how to subtract the scattered light contamination from one of our LIGHTS fields. However, the use of the extended PSFs does not end there, and in future papers, we will show how the LIGHTS extended PSFs can be used to correct for example: a) the effect of the scattered light produced

by the galaxies themselves on the study of the outermost regions of these objects, and b) the effect on the number counts of faint objects detected in the images (particularly those close to the brightest stars).

#### ACKNOWLEDGMENTS

We thank Mohammad Akhlaghi and Sergio Guerra Arencibia for interesting discussions during the development of this work. IT acknowledges support from the ACIISI, Consejería de Economía, Conocimiento y Empleo del Gobierno de Canarias and the European Regional Development Fund (ERDF) under a grant with reference PROID2021010044 and from the State Research Agency (AEI-MCINN) of the Spanish Ministry of Science and Innovation under the grant PID2022-140869NB-I00 and IAC project P/302302, financed by the Ministry of Science and Innovation, through the State Budget and by the Canary Islands Department of Economy, Knowledge, and Employment, through the Regional Budget of the Autonomous Community. RIS acknowledges the funding by the Governments of Spain and Aragon through FITE and Science Ministry (PGC2018-097585-B-C21, PID2021-124918NAC43). GG acknowledges support from IAC project P/302304 and through the IAC project TRACES which is partially supported through the state budget and the regional budget of the Consejeria de Economia, Industria, Comercio y Conocimiento of the Canary Islands Autonomous Community. MM acknowledges support from the project  $P\C$ I2021-122072-2B, financed by MICIN/AEI/10.13039/501100011033, and the European Union "NextGenerationEU"/RTRP, and from the project RYC2022-036949-I financed by the MI-CIU/AEI/10.13039/501100011033 and by FSE+. J.R acknowledges financial support from the Spanish Ministry of Science and Innovation through the project PID2022-138896NB-C55. SR acknowledges the support of the grant PID2023-150393NB-I00 from the Spanish Ministry of Science, Innovation and Universities and SZ acknowledges the support by PID2021-123313NA-I00 of MICIN/AEI/10.13039/501100011033/FEDER, UE.

This research has made use of the Washington Double Star Catalog maintained at the U.S. Naval Observatory.

This research was done with the following free software programs and libraries: 1.23, Bzip2 1.0.8, CFITSIO 4.1.0, CMake 3.24.0, cURL 7.84.0, Dash 0.5.11-057cd65, Discoted flock 0.4.0, Expat 2.4.1, File 5.42, Fontconfig 2.14.0, FreeType 2.11.0, Git 2.37.1, GNU Astronomy Utilities 0.20.27-9b95b (Akhlaghi & Ichikawa 2015b; Akhlaghi 2019), GNU Autoconf 2.71, GNU Automake 1.16.5, GNU AWK 5.1.1, GNU Bash 5.2-rc2, GNU Binutils 2.39, GNU Bison 3.8.2, GNU Compiler Collection (GCC) 12.1.0, GNU Coreutils 9.1, GNU Diffutils 3.8, GNU Emacs 28.1, GNU Findutils 4.9.0, GNU gettext 0.21, GNU gperf 3.1, GNU Grep 3.7, GNU Gzip 1.12, GNU Integer Set Library 0.24, GNU libiconv 1.17, GNU Libtool 2.4.7, GNU libunistring 1.0, GNU M4 1.4.19, GNU Make 4.3, GNU Multiple Precision Arithmetic Library 6.2.1, GNU Multiple Precision Complex library, GNU Multiple Precision Floating-Point Reliably 4.1.0, GNU Nano 6.4, GNU NCURSES 6.3, GNU Readline 8.2-rc2, GNU Scientific Library 2.7, GNU Sed 4.8, GNU Tar 1.34, GNU Texinfo 6.8, GNU Wget 1.21.2, GNU Which 2.21, GPL Ghostscript 9.56.1, Help2man, Less

590, Libffi 3.4.2, Libgit2 1.3.0, libICE 1.0.10, Libidn 1.38, Libjpeg 9e, Libpaper 1.1.28, Libpng 1.6.37, libpthread-stubs (Xorg) 0.4, libSM 1.2.3, Libtiff 4.4.0, libXau (Xorg) 1.0.9, libxcb (Xorg) 1.15, libXdmcp (Xorg) 1.1.3, libXext 1.3.4, Libxml2 2.9.12, libXt 1.2.1, Lzip 1.23, OpenSSL 3.0.5, PatchELF 0.13, Perl 5.36.0, pkg-config 0.29.2, podlators 4.14, Python 3.10.6, util-Linux 2.38.1, util-macros (Xorg) 1.19.3, WCSLIB 7.11, X11 library 1.8, XCB-proto (Xorg) 1.15, xorgproto 2022.1, xtrans (Xorg) 1.4.0, XZ Utils 5.2.5 and Zlib 1.2.11. The IATEX source of the paper was compiled to make the PDF using the following packages: biber 2.19, biblatex 3.19, bitset 1.3, caption 66580 (revision), courier 61719 (revision), csquotes 5.2n, date-

time 2.60, ec 1.0, etoolbox 2.5k, fancyhdr 4.1, fancyvrb 4.5a, fmtcount 3.07, fontaxes 1.0e, footmisc 6.0d, fp 2.1d, helvetic 61719 (revision), hyperref 7.00v, kastrup 15878 (revision), letltxmacro 1.6, logreq 1.0, mweights 53520 (revision), natbib 8.31b, newtx 1.71, pdfescape 1.15, pdf-texcmds 0.33, pgf 3.1.10, pgfplots 1.18.1, preprint 2011, setspace 6.7b, sttools 3.0, tex 3.141592653, texgyre 2.501, times 61719 (revision), titlesec 2.14, trimspaces 1.1, tx-fonts 15878 (revision), ulem 53365 (revision), xcolor 2.14, xkeyval 2.9 and xstring 1.85. We are very grateful to all their creators for freely providing this necessary infrastructure. This research (and many other projects) would not be possible without them.

#### REFERENCES

```
Akhlaghi M., 2019, arXiv e-prints, p. arXiv:1909.11230
Akhlaghi M., Ichikawa T., 2015a, The Astrophysical Journal
  Supplement Series, 220, 1
Akhlaghi M., Ichikawa T., 2015b, ApJS, 220, 1
Borlaff A., Marcum P., 2022, in American Astronomical Society
  Meeting #240. p. 304.06
Borlaff A., et al., 2019, A&A, 621, A133
Capaccioli M., et al., 2015, A&A, 581, A10
Chamba N., Trujillo I., Knapen J. H., 2022, A&A, 667, A87
Duc P.-A., et al., 2015, MNRAS, 446, 120
Euclid Collaboration et al., 2024, arXiv e-prints, p.
  arXiv:2405.13491
Ferrarese L., et al., 2012, ApJS, 200, 4
Fliri J., Trujillo I., 2016, MNRAS, 456, 1359
Gaia Collaboration et al., 2021, A&A, 649, A1
Giallongo E., et al., 2008, A&A, 482, 349
Golini G., Montes M., Carrasco E. R., Román J., Trujillo I., 2024,
  A&A, 684, A99
Haigh C., Chamba N., Venhola A., Peletier R., Doorenbos L.,
  Watkins M., Wilkinson M. H. F., 2021, A&A, 645, A107
Hood C. E., Kannappan S. J., Stark D. V., Dell'Antonio I. P.,
  Moffett A. J., Eckert K. D., Norris M. A., Hendel D., 2018,
  ApJ, 857, 144
Huang S., et al., 2018, MNRAS, 480, 521
Infante-Sainz R., Akhlaghi M., 2024, Research Notes of the
  American Astronomical Society, 8, 10
Infante-Sainz R., Trujillo I., Román J., 2020, Monthly Notices of
  the Royal Astronomical Society, 491, 5317
Infante-Sainz R., Akhlaghi M., Eskandarlou S., 2024, Research
  Notes of the American Astronomical Society, 8, 22
Laine S., et al., 2018, arXiv e-prints, p. arXiv:1812.04897
```

This paper was built using the Open Journal of Astrophysics IATEX template. The OJA is a journal which

Mancera Piña P. E., Golini G., Trujillo I., Montes M., 2024,

Martín-Navarro I., Trujillo I., Knapen J. H., Bakos J., Fliri J.,

Martínez-Lombilla C., Trujillo I., Knapen J. H., 2019, MNRAS,

A&A, 689, A344

483, 664

2014, MNRAS, 441, 2809

```
Mason B. D., Wycoff G. L., Hartkopf W. I., Douglass G. G.,
  Worley C. E., 2012, VizieR Online Data Catalog: The
  Washington Visual Double Star Catalog (Mason+ 2001-2012),
  VizieR On-line Data Catalog: B/wds. Originally published in:
  2001AJ....122.3466M
Merritt A., van Dokkum P., Abraham R., Zhang J., 2016, ApJ,
  830, 62
Mihos J. C., Harding P., Spengler C. E., Rudick C. S., Feldmeier
  J. J., 2013, ApJ, 762, 82
Montes M., Brough S., Owers M. S., Santucci G., 2021, The
  Astrophysical Journal, 910, 45
Montes M., et al., 2024, A&A, 681, A15
Oke J., Gunn J., 1983, Astrophysical Journal, Part 1, vol. 266,
  Mar. 15, 1983, p. 713-717., 266, 713
Rich R. M., et al., 2019, MNRAS, 490, 1539
Román J., Trujillo I., Montes M., 2020, Astronomy &
  Astrophysics, 644, A42
Román J., Castilla A., Pascual-Granado J., 2021, A&A, 656, A44
Román J., et al., 2023, A&A, 679, A157
Sandin C., 2014, Astronomy & Astrophysics, 567, A97
Slater C. T., Harding P., Mihos J. C., 2009, Publications of the
  Astronomical Society of the Pacific, 121, 1267
Trujillo I., Bakos J., 2013, MNRAS, 431, 1121
Trujillo I., Fliri J., 2016, The Astrophysical Journal, 823, 123
Trujillo I., Aguerri J. A. L., Cepa J., Gutiérrez C. M., 2001a,
  MNRAS, 321, 269
Trujillo I., Aguerri J. A. L., Cepa J., Gutiérrez C. M., 2001b,
  MNRAS, 328, 977
Trujillo I., Chamba N., Knapen J. H., 2020, MNRAS, 493, 87
Trujillo I., et al., 2021, Astronomy & Astrophysics, 654, A40
Watkins A. E., Kaviraj S., Collins C. C., Knapen J. H., Kelvin
  L. S., Duc P.-A., Román J., Mihos J. C., 2024, MNRAS, 528,
York D. G., et al., 2000, AJ, 120, 1579
Zaritsky D., et al., 2024, AJ, 168, 69
```

provides fast and easy peer review for new papers in the astro-ph section of the arXiv, making the reviewing process simpler for authors and referees alike. Learn more at http://astro.theoj.org.

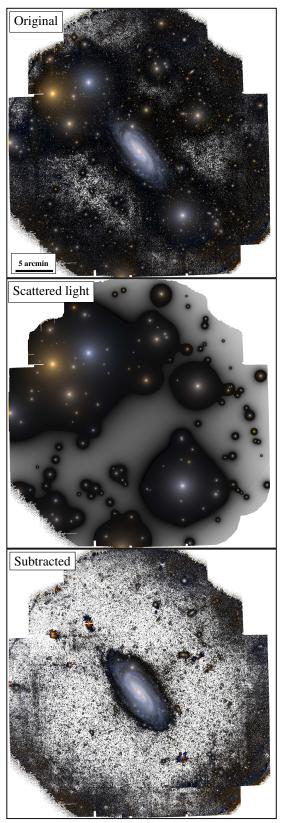


FIG. 12.— Colour composite image of the LIGHTS field NGC3198, using g and r Sloan filters. The figure has been created using astscript-color-faint-gray (Infante-Sainz & Akhlaghi 2024). Upper panel: original image. Note the enormous contamination caused by the scattered light from the brightest stars at the edge of the central galaxy. Middle panel: modelling of the scattered light field of all stars brighter than 17 mag (G-band). Bottom panel: the field of LGHTS NGC3198 after removing the scattered light field. The outermost parts of the central galaxy are now better defined, allowing more accurate analysis of this region.

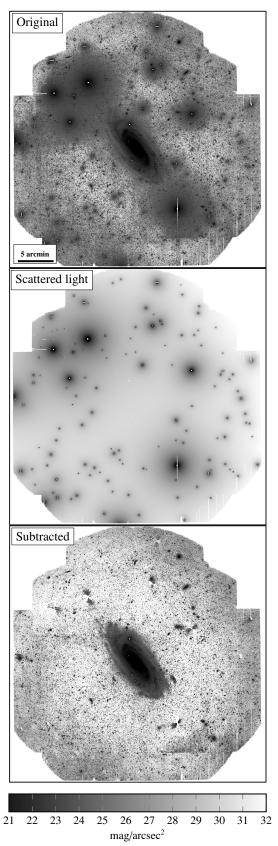


Fig. 13.— Similar to Fig. 12 but for the g-band only. The scattered light map in the middle panel shows that the contribution of the scattered light from the brightest stars in the field to the central region of the image is  $28.9~\mathrm{mag/arcsec^2}$ .

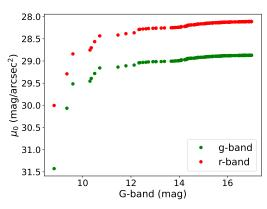


Fig. 14.— The contribution of scattered light to the surface brightness at the centre of the image as the number of stars modelled increases by adding fainter stars. The surface brightness at the location of the main galaxy (here labeled as  $\mu_0$ ) becomes brighter as fainter and fainter stars are modelled. In this particular field, modelling the scattered light of stars fainter than 16 mag (G-band) barely changes the central surface brightness of the image by less than 3%.